Available online at www.sciencedirect.com

SciVerse ScienceDirect

Ceramics International 39 (2013) 1233–1240

CERAMICS INTERNATIONAL

www.elsevier.com/locate/ceramint

Thermal and dynamic mechanical analyses on $Bi_{0.5}Na_{0.5}TiO_3$–$BaTiO_3$ ceramics synthesized with citrate method

Xiu-Cheng Zheng, Guang-Ping Zheng*, Zheng Lin, Zhi-Yuan Jiang

Department of Mechanical Engineering, The Hong Kong Polytechnic University, Hong Kong

Received 14 June 2012; received in revised form 13 July 2012; accepted 13 July 2012
Available online 24 July 2012

Abstract

$Bi_{0.5}Na_{0.5}TiO_3$–$xBaTiO_3$ (BNT–xBT) nano-powders are successfully synthesized by a modified citrate method. The as-prepared BNT-BT powders and the sintered ceramics are homogeneous with a pure perovskite crystal structure. The effects of Ba^{2+} substitutions for $(Bi_0.5Na_{0.5})^{2+}$ in the A-sites of $Bi_{0.5}Na_{0.5}TiO_3$ on its phase transformations are explored. The transformations among ferroelectric (FE), anti-ferroelectric (AFE) and paraelectric (PE) states in these ceramics are characterized using ferroelectric hysteresis tests, modulated differential scanning calorimetry and dynamic mechanical analysis. The FE-AFE transition in BNT–xBT with $0 \le x \le 0.15$ is found to relate with a structural transformation which is a first-order phase transition. The mechanical and thermal analyses provide evidence that AFE state ($0 \le x \le 0.15$) could be associated with the incommensurate modulation of rhombohedral structures while the mechanisms of forming AFE state in BNT–xBT ($x > 0.15$) could be different.

Keywords: Lead-free ferroelectric ceramics; Citrate method; Phase transformation; Elasticity anomaly

1. Introduction

Lead-based ferroelectrics, e.g., lead zirconate titanate ($Pb(Zr, Ti)O_3$ or PZT) are the most widely used materials for piezoelectric actuators, sensors and transducers [1]. Due to lead toxicity, there are growing concerns on the processing, the use and the disposal of devices containing PZT. Hence developing piezoelectric materials that are biocompatible and environmentally friendly [2] is of great interest. It is known that bismuth sodium titanate ($Bi_{0.5}Na_{0.5}TiO_3$, abbreviated as BNT) is one of the most important lead-free piezoelectric materials with a perovskite structure. It has a high Curie temperature ($Tc = 320$ °C) and a large remanent polarization (Pr $\sim 38\ \mu C/cm^2$) at room temperature. Although BNT has been considered as a promising candidate to replace the widely used lead-based piezoelectric materials [3], the large coercive field (Ec ~ 73 kV/cm), low de-poling temperature, and high conductivity during poling have hindered it from wide-spread applications [4].

To improve the piezoelectric properties, a number of BNT-based solid solutions, such as BNT–$Bi_{0.5}K_{0.5}TiO_3$ [5], BNT–$NaNbO_3$ [6], BNT–$Bi_{0.5}K_{0.5}TiO_3$–$Bi_{0.5}Li_{0.5}TiO_3$ [7], BNT–$BaTiO_3$–$Bi_{0.5}Li_{0.5}TiO_3$ [8], and BNT–$Bi_{0.5}K_{0.5}TiO_3$–$BaTiO_3$ [9] have been developed and studied intensively. It is noteworthy that BNT-based piezoelectric shows high strain when the A-site is slightly substituted by Ba^{2+} and the addition of $BaTiO_3$ to BNT may improve the piezoelectric and sintering properties [10–12]. At room temperature, BNT has a rhombohedral symmetry and $BaTiO_3$ has a tetragonal symmetry, resulting in a rhombohedral–tetragonal morphotropic phase boundary (MPB) for their solid solution. Compared with BNT, the BNT–$xBaTiO_3$ (abbreviated as BNT–xBT) whose composition is near such phase boundary ($x \sim 0.06$) shows a substantially improved poling behavior and piezoelectric properties [13]. At elevated temperature, BNT–xBT changes from a ferroelectric (FE) states to an anti-ferroelectric (AFE) states before it becomes paraelectric (PE) at higher

---

*Corresponding author.
E-mail address: mmzheng@polyu.edu.hk (G.-P. Zheng).

0272-8842/$ - see front matter © 2012 Elsevier Ltd and Techna Group S.r.l. All rights reserved.
http://dx.doi.org/10.1016/j.ceramint.2012.07.052

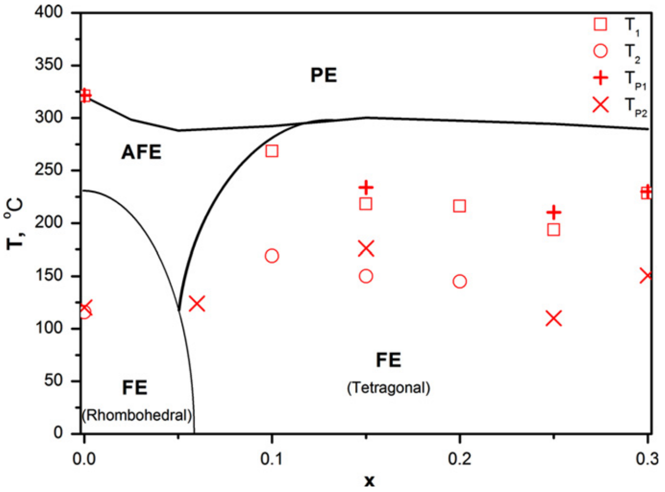

Fig. 1. Phase diagram of BNT–*x*BT. The solid curves are schematic of phase boundaries given in Ref. [14]. The symbols are the structural transformation temperatures determined from DSC and DMA analyses in this work.

temperature. Fig. 1 is the schematic [14] showing the phase diagram of BNT–*x*BT.

To date, most of the BNT and BNT-based ceramics are made from powders prepared by the conventional solid-state method. However, the as-prepared powders by the solid-state method consist of rather coarse, poorly uniform particles with board particles size distributions [15]. The citrate method is a kind of sol–gel method using citric acid as a complexing agent. The complexing of metal cations by free carboxyl groups allows molecular-level mixing of the reactants and leads to uniform, fine powders with a high purity at relatively low temperatures. Xu et al. [13] found the citrate method is an advantageous alternative route compared with the conventional method in producing BNT–*x*BT ceramics. The ceramics made by the citrate method exhibit superior piezoelectric properties near the rhombohedral-tetragonal morphotropic phase boundary. However, the investigation on this topic is mainly limited to the nominal composition of $(Bi_{0.5}Na_{0.5})_{1-x}Ba_xTiO_3$ ($x=0$, 0.02, 0.04, 0.06, 0.08, 0.10, 0.12) with a mole ratio of citric acid to total metal cation content (C/M) of 1.25. It is necessary to prepare BNT–*x*BT ceramics with a wider composition using the citrate method to obtain superior ferroelectric properties.

Although the transformations among ferroelectric (FE), anti-ferroelectric (AFE) and paraelectric (PE) states in these ceramics have been extensively investigated, there are still considerable debates on the structural origin of the AFE states or relaxor ferroelectric properties in BNT–*x*BT near the MPB. One viewpoint on the nature of FE-AFE transition is that the transition is simply the polar-unpolar changes of domains at elevated temperature and no structural transformation is involved during the FE-AFE transition [16]. Another viewpoint is based on transmission electron microscopy and neutron scattering studies [17], which ascribes the FE-AFE transition to the incommensurate modulation of rhombohedral and tetragonal structures. Thermal and dynamic mechanical analyses are very sensitive to the structural changes of materials and could provide useful information on the structural origin of the FE-AFE transition. But to date these analysis techniques have not been systematically used to resolve the nature of FE-AFE transition in BNT–*x*BT ceramics.

Thus, in this study, we first prepare $(Bi_{0.5}Na_{0.5})_{1-x}Ba_xTiO_3$ ($x=0.05$, 0.06, 0.07, 0.08, 0.10, 0.15, 0.20, 0.25, 0.30) powders with $C/M=1.60$ by the citrate method. The as-prepared BNT-BT powders and the corresponding ceramics are characterized by using various techniques. In addition, the ferroelectric properties and phase transformations of the ceramics are investigated using ferroelectric hysteresis tests, temperature modulated differential scanning calorimetry (TM-DSC) and dynamic mechanical analysis. The analyses will provide deep insights into transformations among ferroelectric (FE), anti-ferroelectric (AFE) and paraelectric (PE) states in these ceramics.

2. Preparation of BNT–*x*BT using citrate method

Reagent-grade $NaNO_3$, $Ba(NO_3)_2$, $Bi(NO_3)_3 \cdot 5H_2O$, citric acid and tetrabutyl titanate were used as starting materials to prepare BNT–*x*BT powders with the nominal composition of $(Bi_{0.5}Na_{0.5})_{1-x}Ba_xTiO_3$ ($x=0.05$, 0.06, 0.07, 0.08, 0.10, 0.15, 0.20, 0.25, 0.30) by the citrate method. The mole ratio of citric acid to total metal cation content (abbreviated as C/M) was 1.60. A weighted amount of citric acid was first dissolved into deionized water. An appreciate amount of aqueous ammonia was dripped to adjust the pH value of the solution to about 8.5. Then, a designed amount of tetrabutyl titanate was slowly added to the flask reactor fitted with a reflux condenser under stirring. After the stirring at 60 °C for 2.5 h, a yellowish two-layer liquid was obtained, comprising a transparent aqueous solution in addition to an oil-like liquid on the top layer. The aqueous solution was separated from the mixing liquid. Various nitrates were added into the solution according to the nominal composition of the powders, following by stirring at 92 °C for 5 h to generate a transparent, yellowish precursor solution. The pH value of the solution was about 6–7. The precursor solution was dehydrated in an oven at 105 °C to form a sol. Subsequent heating at a higher temperature of 160 °C yielded a black gel. The gel was pulverized and then calcined at 280 °C for 1 h and 600 °C for 2 h in air. The as-obtained samples are designated as BNT–*x*BT, where x stands for the composition of BT ($x=0.05$, 0.06, 0.07, 0.08, 0.10, 0.15, 0.20, 0.25, 0.30, respectively).

The mole ratio of citric acid to total metal cation content is a key factor to the formation of the BNT–*x*BT sol and gel in the preparation process of citrate method. Xu et al. [13] found the C/M in the range 1.2–1.6 may produce a homogeneous, transparent sol and gel when the finical stirring reaction temperature was 80 °C. In this study, we found the white precipitate still appeared in the sol even the C/M value was 1.6 when the finical stirring reaction temperature was

80 °C. When the finical stirring reaction temperature was increased to 92 °C, the white precipitate disappeared. Such difference may be due to different starting materials or reaction.

The prepared BNT–*x*BT powders were pressed at a pressure of 750 MPa in the form of disks. The disks were 13 mm in diameter and 1.5 mm in thickness. The green disks were heated at 600 °C for 6 h to remove the polyvinyl alcohol binder. The calcined disks were sintered at 1100 °C in ambient atmosphere for 2 h to form the ceramics.

3. Characterization of samples' structural and ferroelectric properties

The crystalline structure of the ceramics were determined by X-ray diffraction with a Bruker D8 advance diffractometer using Co K_α radiation ($\lambda = 1.79021$ Å). The microstructures of as-prepared ceramic materials were investigated by using a scanning electron microscopy (SEM, JEOL model JSM-6490, secondary electron image at 20 kV). The specific surface area of the BNT-BT powders was determined by the Brunauer–Emmett–Teller (BET) method from N_2 adsorption and desorption isotherms at 77 K on a Quantachrome NOVA 1000e surface area & pore size analyzer.

Fig. 2 shows the X-ray diffraction (XRD) patterns of the as-prepared BNT–*x*BT ($x = 0.05$) powders calcined at different temperatures. It can be found that only a pure perovskite phase is certified after calcining at 600 °C. When the temperature is increased to 650–800 °C, the other unidentified phase appears. These peaks may be attributed to $Bi_4Ti_3O_{12}$, Bi_2O_3, or TiO_2 [11,13]. Therefore in this work, 600 °C is chosen as the preferred calcining temperature for the BNT–*x*BT powders.

Fig. 3 shows the XRD patterns of ceramics with different mole ratio of BNT to BT, respectively. It can be found in Fig.3 that only a perovskite phase is certified and no second phases could be detected, indicting that Ba^{2+} diffuses into the $Bi_{0.5}Na_{0.5}TiO_3$ lattice to form a homologous solid solution. The results indicate that the citrate method used in this work is effective in preparing BNT–*x*BT ferroelectric ceramics with a single perovskite phase.

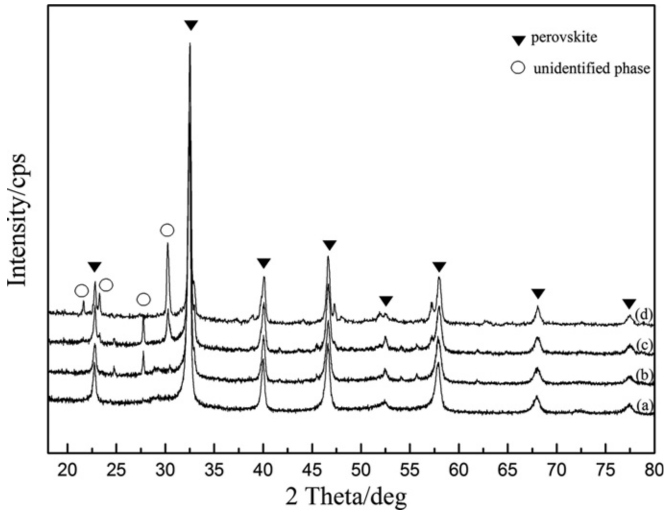

Fig. 2. XRD patterns of the BNT–*x*BT ($x = 0.05$) powders calcined at different temperatures: (a) 600 °C; (b) 650 °C; (c) 700 °C; (d) 800 °C.

Furthermore, it is shown clearly in Fig. 3 that the (1 1 0) peak moves to lower angle, especially when the BT ratio *x* is in the range of 0.20–0.30, with the increase of BT ratio *x* in the obtained ceramics, indicating that the size of the perovskite unit cell increases with the increasing BT ratio. This is due to the fact that the ionic radius of Ba^{2+} (0.135 nm) is larger than those of Na^{+}(0.097 nm) and Bi^{3+}(0.096 nm). When Na^{+} or Bi^{3+} is replaced by Ba^{2+}, the lattice cell is enlarged. As a result, the corresponding XRD peak moves to lower angle.

Rhombohedral symmetry of pure BNT at room temperature is characterized by a (0 0 3)/(0 2 1) peak splitting between 38° and 42° and a single (2 0 2) peak at about 46.8° detected with Cu K_α. Considering the gradual evolution of the XRD patterns from the (2 0 2) peak to a (0 0 2)/(2 0 0) peak splitting, corresponding to a tetragonal symmetry, it is argued that [18] the splitting of the peak could be ascribed to the simultaneous diffraction of the (0 0 2)/(2 0 2)/(2 0 0) planes and the relative content of rhombohedral phase is gradually reduced with increasing concentration of BT. In our studies XRD patterns of BNT–*x*BT ceramics in the *2 thetra* range of 51–57° detected with Co K_α are shown in Fig. 3. As it can be seen that the strength of (2 0 0) peak reduces with increasing BT ratio *x*. While the strength of (0 0 2) peak increases with the increase of BT ratio, especially in the BNT–0.3BT case. Thus we might make a similar conclusion as those of previous studies [18]: When the BT ratio is lower than 0.2, the main crystal phase is rhombohedral; When the BT ratio increases further, more and more crystals with tetragonal phase appear and there is not rhombohedral phase in BNT–*x*BT when $x \geq 0.2$.

Table 1 shows the microstructure parameters of the as-prepared BNT–*x*BT powders. These powders exhibit similar specific surface areas (4.9–6.3 $m^2\,g^{-1}$). On the other hand, the average crystallite size decreases obviously with the increase of BT contents. One can see that the crystallite size of BNT–0.05BT powder is 25.9 nm. While it decreases to 10.0 nm of the powder sample of BNT–0.3BT. The nano-powders enable us to sinter BNT–*x*BT ceramics with good quality. For example, the density of BNT–0.06BT is 5.6 g/cm^3 which is close its theoretical density.

The P–E loops of the sintered BNT–*x*BT ceramics measured with a ferroelectric test system (TF Analyzer 2000E, aixACCT) are shown in Fig. 4(a). All the ceramics exhibit typical ferroelectric hysteresis. The remanent polarization and coercive field for these specimens are determined from the P–E loops. Table 1 lists the ferroelectric properties of the sintered BNT–*x*BT ceramics. We can observe that the BT content influences the ferroelectric properties significantly. With the increase of BT contents in the sintered BNT–*x*BT ceramics, *Ec* may decrease and *Pr* may increase. BNT–0.06BT exhibits a remanent

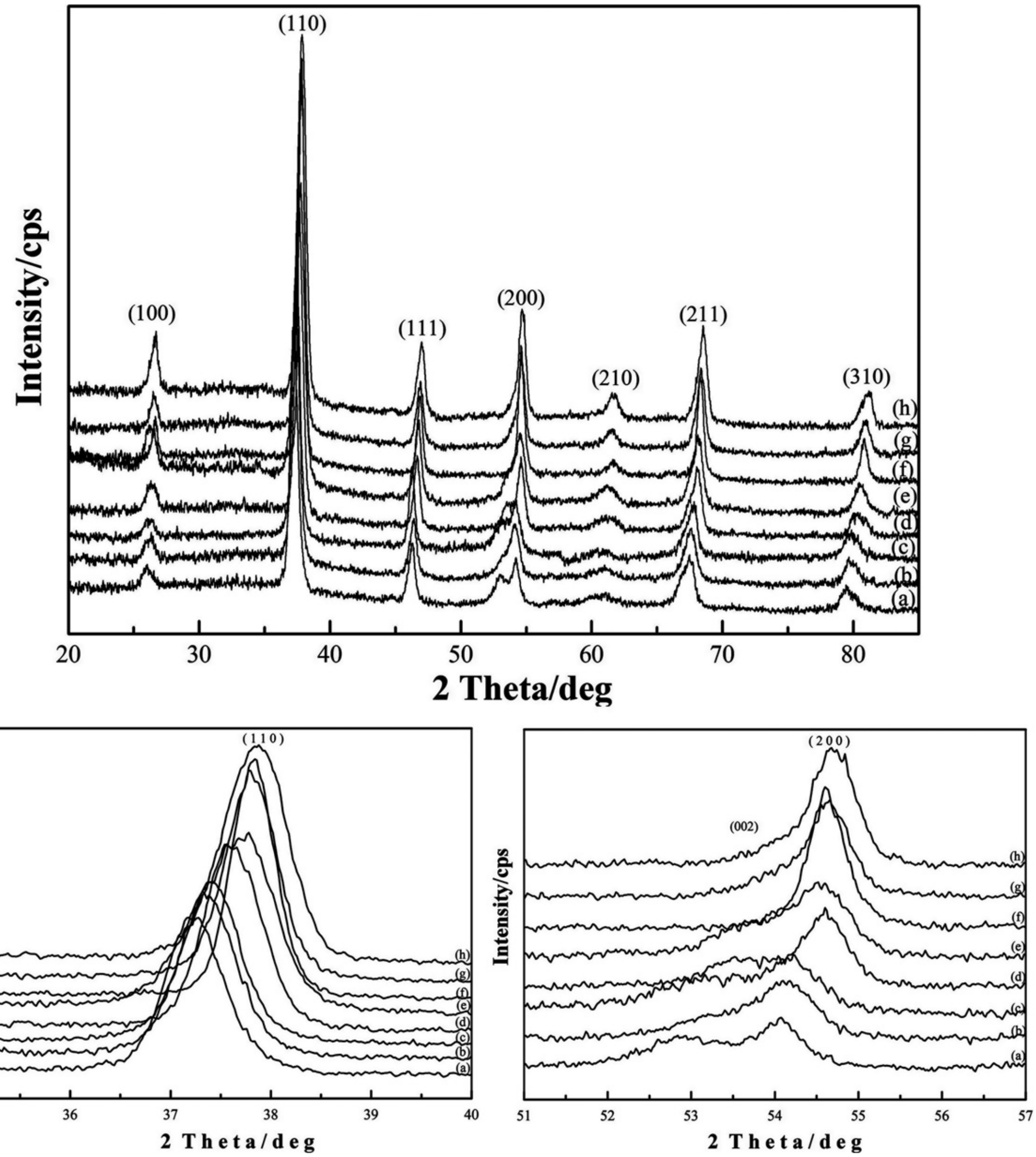

Fig. 3. XRD patterns of the sintered BNT–*x*BT ceramics: (a) $x=0.30$; (b) $x=0.25$; (c) $x=0.20$; (d) $x=0.15$; (e) $x=0.10$; (f) $x=0.08$; (g) $x=0.06$; (h) $x=0.05$.

Table 1
Surface areas *A* and crystallite sizes *d* of the as-prepared BNT–*x*BT powders, and grain sizes *D*, coercive fields E_c and remanent polarizations P_r of the sintered ceramics.

x	0.05	0.06	0.07	0.08	0.1	0.15	0.2	0.25	0.3
A(m^2/g)	5.9	5.2	4.9	5.3	5.7	5.9	5.5	6.3	5.1
***d* (nm)**	25.9	23.0	21.2	19.7	18.4	11.8	11.2	10.6	10.0
***D* (μm)**	1.74				1.16	1.06	0.90	0.75	
E_c (kV/cm)	28.3	39.8	16.9	18.8	34.8	37.3	31.0	23.5	21.8
P_r (μC/cm^2)	20.8	26.3	9.7	13.5	17.5	31.7	11.0	29.8	25.0

polarization (*Pr*) of 39.8 μC/cm^2 and a relatively low coercive field (*E*c) of 26.3 kV/cm. In all the ceramic samples prepared under the reaction condition reported in this paper, BNT–0.06BT exhibits relatively good ferroelectric properties. AFE state in BNT–0.06BT is confirmed by measuring the P–E loops at different temperatures. As shown in Fig. 4(b), the FE-AFE transition in BNT–0.06BT occurs at about 125 °C.

4. Thermal and dynamic mechanical analyses on BNT–*x*BT

4.1. DSC analyses on phase transformations

Thermal analysis of BNT–*x*BT ceramics was performed using DSC (model Q200, TA Instruments). Fig. 5(a)–(b) show the DSC curves of BNT–*x*BT with $x=0$, 0.1, 0.15, 0.2, 0.25 and 0.3. DSC curves of BNT–*x*BT with $x=0.05$, 0.06, 0.07, 0.08 are not shown since they are continuous and smooth from −10 °C to 400 °C. There are two peaks in a DSC curve of BNT–*x*BT with $x=0$, 0.1, 0.15, 0.2. Based on the schematic [14] of phase diagram shown in Fig. 1, the endothermal peak at higher temperature should reflect the transition from an anti-ferroelectric (AFE) state to

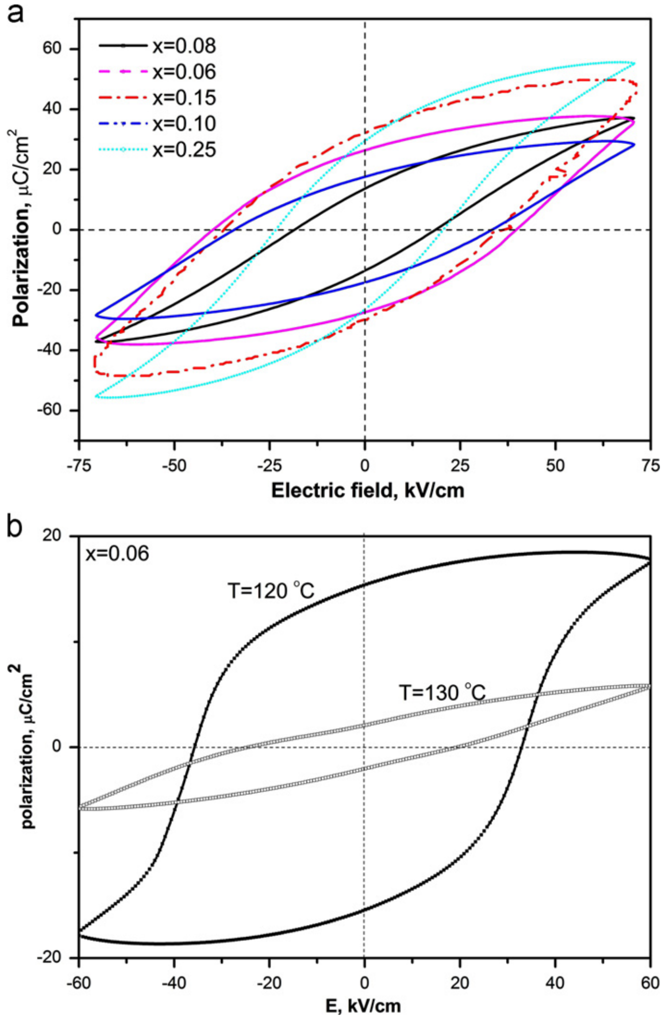

Fig. 4. (a) P–E hysteresis loops of the BNT–xBT ceramics. (b) P–E loops of BNT–0.06BT at different temperatures.

a paraelectric (PE) state with a peak temperature denoted as T_1. There is a board peak indicating an endothermal process of these samples at lower temperature, whose peak temperature is denoted as T_2 after subtracting the backgrounds. The peak at T_2 is further investigated using temperature modulated DSC (TM-DSC). Fig. 5(c) shows the TM-DSC results in BNT–0.15BT as an example. The heat capacity anomalies at T_2 and T_1 do not shifted with the periods of the modulated temperature, suggesting that the transition at T_2 is also a structural transformation. T_1 and T_2 of various BNT–xBT samples determined from the TM-DSC results on heat capacity are listed in Table 2. Table 2 also lists T_1 of BNT–xBT with $x=0.25$ and 0.3. But the T_2 of these two samples are difficult to be determined from the TM-DSC results and are not listed.

4.2. DMA analyses on structural transformations

Anelastic mechanical test of the BNT–xBT is performed using Dynamic Mechanical Analyzer (DMA, model Q800, TA Instruments). Samples are tested in a three-point bending mode. Fig. 6(a) shows the storage modulus and mechanical loss tanδ (or internal friction Q^{-1}) results of BNT with a heating rate of 0.6 K/min. Clearly there are two peaks in the tanδ curve with their peak temperatures denoted as T_{p1} and T_{p2} ($<T_{p1}$), respectively. $T_{p1}=321.6$ °C and $T_{p2}=124.2$ °C in BNT. There are elastic softening behaviors of BNT around T_{p1} and T_{p2} in the storage modulus curves. In addition T_{p1} and T_{p2} are almost independent of frequency, but show hysteresis upon heating and cooling (not shown). The DMA results suggest that there are structural transformations around these two temperatures, and they are different in transformation mechanisms. The height of tanδ peak at T_{p1} increases with decreasing frequency and the lattice (elastic) softening occurs right at T_{p1}, indicating the ferroelastic nature of this structural transformation. The tanδ peak at T_{p2} does not show these features. Instead, the height of tanδ peak at T_{p2} is slightly dependent on frequency, and the lattice softening occurs at a temperature higher than T_{p2}. These characteristics of internal friction and modulus softening are similar with those of a commensurate–incommensurate phase transition [19].

Fig. 6(b)shows the DMA results of BNT–0.06BT. The internal friction and modulus softening around $T_{p2}=123.9$ °C show the same features as those in BNT. However, the internal friction peak and elastic anomaly occurs around $T_{p1}=374.5$ °C show significant relaxation features and are much different with those in BNT.

Fig. 6(c) shows the DMA results of BNT–0.15BT. The internal friction peak at $T_{p2}=176.2$ °C merges with that at $T_{p1}=233.9$ °C. After fitting the background of internal friction below T_{p1} using a Gaussian function, the internal friction peak can be separated and is shown in the inset. The peak temperature T_{p2} is found to be independent of frequency. From the DMA results, it can be found that the structural transformations in BNT–0.15BT around T_{p1} and T_{p2} are first-order transformations and are similar with those in BNT in transformation mechanisms.

Fig. 6(d) shows the DMA results of BNT–0.25BT. The internal friction peak which occurs at $T_{p1}=210.3$ °C has similar features as those in BNT–xBT with $x=0$, 0.15. It seems that there is an internal friction peak around $T_{p2}=110$ °C which shows relaxation feature. The internal friction peaks occurs in BNT–0.3BT show similar behaviors as those of BNT–0.25BT and the DMA results are not shown here.

4.3. Discussions

Based on the schematic [14] of phase diagram shown in Fig. 1, the structural transformation around T_2 or T_{p2} should reflect the transition from a ferroelectric (FE) state to an AFE state. Hence the T_2 determined from DSC and T_{p2} determined from DMA would allow us to accurately describe the phase boundary between FE and AFE states in the phase diagram. As shown in Fig. 1, the transition temperature of this FE-AFE transition determined from DSC results (T_2) is consistent with that from DMA results (T_{p2}). Combined the DSC and DMA results with the XRD

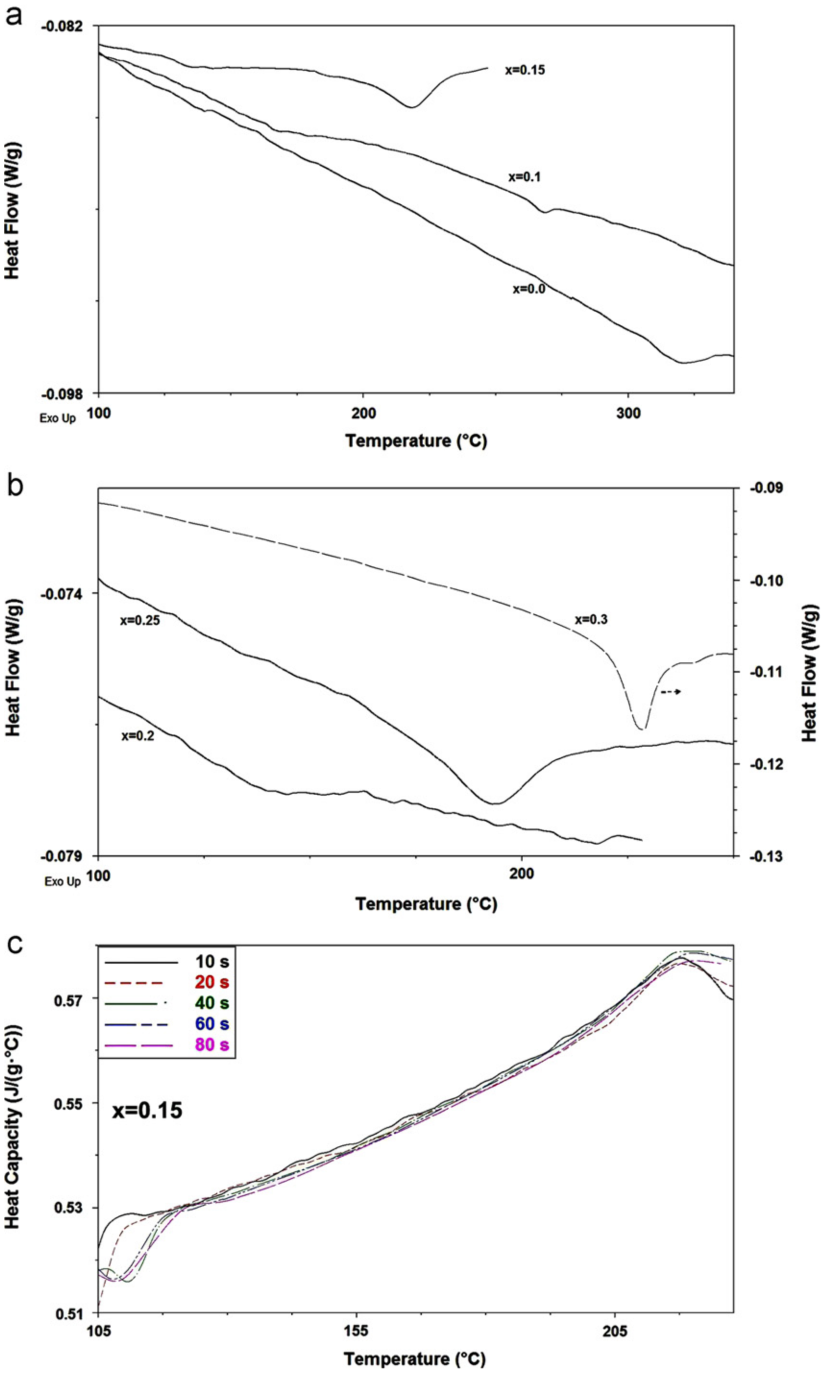

Fig. 5. (a) and (b): DSC heat flows of BNT–xBT. The heating rate is 10 K/min. (c) Heat capacity of BNT–0.15BT with different TM-DSC periods. The heating rate is 5 K/min. The amplitude of the modulated temperature is 2 °C.

results, the nature of such FE-AFE transition could be explored. In BNT–xBT with $0 \leq x \leq 0.15$, there are rhombohedral structures at low temperature according to the XRD results. Thus in the transition region around T_2 or T_{p2}, the structural transformation occurs most likely through cation displacements in the rhombohedral structure to form an incommensurate modulated rhombohedral structure [17]. While for BNT–xBT with $x \geq 0.2$, there is no rhombohedral structure at low temperature. The FE-AFE transition could be caused by a transformation mechanism different with the commensurate-incommensurate transformation, as reflected in the relaxation feature of internal friction peaks around T_{p2}. Detailed investigation will be published elsewhere.

Based on the DSC and DMA analyses, we could accurately describe the FE, AFE and PE states in the phase diagram of BNT–xBT using the phase boundaries defined by T_{p2} (or T_2) and T_{p1} (or T_1), as shown in Fig. 1. The DSC and DMA analyses provide deep insights into the structural origin of FE-AFE transition especially in the

Table 2
Phase transformation (peak) temperatures of BNT–xBT determined from DSC (T_1, T_2) and DMA (T_{p1}, T_{p2}) analyses.

Temperature (°C)	$x=0$	$x=0.06$	$x=0.1$	$x=0.15$	$x=0.2$	$x=0.25$	$x=0.3$
T_1	321.0	♯	268.5	218.2	216.2	193.6	228.5
T_2	115.8	♯	169.0	150.0	144.9	♯	♯
T_{P1}	321.6	374.5*		233.9		210.3	230.1
T_{P2}	120.2	123.9		176.2		110.0*	150.7*

*Indicates the transition temperature is determined from the relaxation peak at $f=0.1$ Hz.
♯Indicates that the transition temperature cannot be determined from DSC analysis.

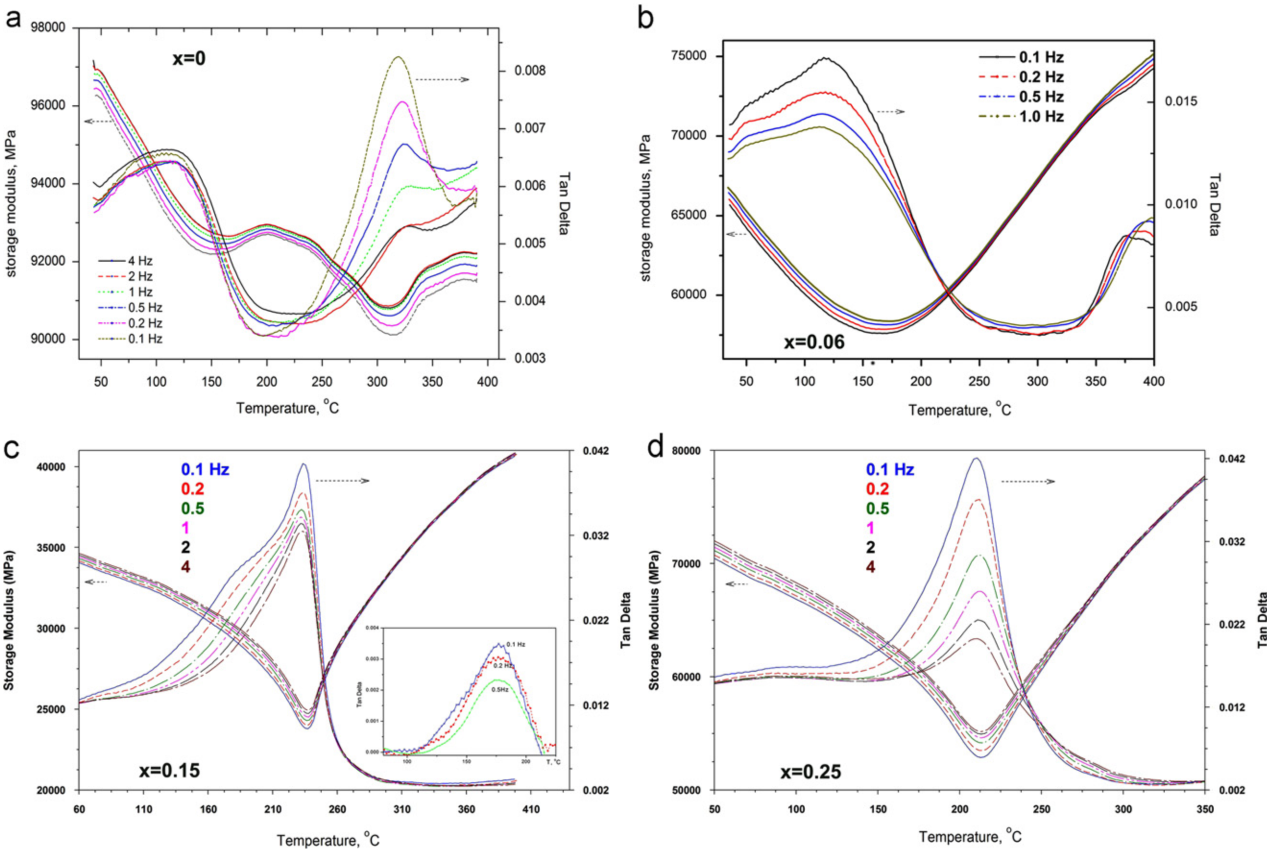

Fig. 6. Storage modulus and internal friction of BNT–xBT under different frequencies of dynamic mechanical tests. (a) $x=0$. (b) $x=0.06$. (c) $x=0.15$. (d) $x=0.25$.

region of $x>0.06$, which has not been fully resolved to date.

5. Conclusions

$Bi_{0.5}Na_{0.5}TiO_3$–$x$$BaTiO_3$ (BNT–xBT) powders with $x=0.05$, 0.06, 0.07, 0.08, 0.10, 0.15, 0.20, 0.25, 0.30 have been successfully fabricated by a modified citrate method. DSC and DMA analyses are used to characterize the structural origin of transitions among FE, AFE and PE states in the phase diagram of BNT–xBT. The FE-AFE transition in BNT–xBT with $0 \leq x \leq 0.15$ is found to relate with a structural transformation which is a first-order phase transition. The mechanical and thermal analyses provide evidences that AFE state ($0 \leq x \leq 0.15$) could be associated with the incommensurate modulation of rhombohedral structure, while the mechanisms of forming AFE state in BNT–xBT ($x>0.15$) could be different.

Acknowledgements

The authors are grateful for the financial supports provided by the Innovative Technology Funds (Project No. ITS314/09) of Hong Kong SAR, China, and the Research Funds of Hong Kong Polytechinc University (Project No. A-PK81).

References

[1] R. Moazzami, C. Hu, W.H. Shepherd, Electrical characteristics of ferroelectric PZT thin films for DRAM applications, IEEE Transactions on Electron Devices 39 (1992) 2044–2049.

[2] Y. Saito, H. Takao, T. Tani, T. Nonoyama, K. Takatori, T. Homma, T. Nagaya, M. Nakamura, Lead-free piezoceramics, Nature 432 (2004) 84–87.

[3] G.A. Smolensky, V.A. Isopov, A.I. Argranovskaya, N.N. Krainic, New ferroelectrics of complex composition IV, Soviet Physics Solid State 2 (1961) 2651–2654.

[4] T. Takenaka, T. Okuda, K. Takegahara, Lead-free piezoelectric ceramics based on $\mathrm{(BiNa)_{1/2}TiO_3}$–$\mathrm{NaNbO_3}$, Ferroelectrics 196 (1997) 175–178.

[5] K. Yoshii, Y. Hiruma, H. Nagata, T. Takenaka, Electrical properties and depolarization temperature of (Bi1/2Na1/2)TiO3–(Bi1/2K1/2)TiO3 lead-free piezoelectric ceramics, apanese Journal of Applied Physics 45 (2006) 4493–4496.

[6] Y.M. Li, W. Chen, J. Zhou, Q. Xu, H.J. Sun, R.X. Xu, Dielectric and piezoelecrtic properties of lead-free (Na0.5Bi0.5)TiO3–NaNbO3 ceramics, Materials Science and Engineering B 112 (2004) 5–9.

[7] Z. Yang, Y. Hou, H. Pan, Y. Chang, Structure, microstructure and electrical properties of $(1-x-y)\mathrm{Bi_{0.5}Na_{0.5}TiO_3}$–$x\mathrm{Bi_{0.5}K_{0.5}TiO_3}$–$y\mathrm{Bi_{0.5}Li_{0.5}TiO_3}$ lead-free piezoelectric ceramics, Journal of Alloys and Compounds 480 (2009) 246–253.

[8] D. Lin, D. Xiao, J. Zhu, P. Yu, Piezoelectric and ferroelectric properties of lead-free. [Bi1 − y(Na1 − x − yLix)]0.5BayTiO3 ceramics, Journal of the European Ceramic Society 26 (2006) 3247–3251.

[9] J. Shieh, K.C. Wu, C.S. Chen, Switching characteristics of MPB compositions of (Bi0.5Na0.5)TiO3–BaTiO3-(Bi0.5K0.5)TiO3 lead-free ferroelectric ceramics, Acta Materialia 55 (2007) 3081–3087.

[10] M. Cernea, E. Andronescu, R. Radu, F. Fochi, C. Galassi, Sol–gel synthesis and characterization of $\mathrm{BaTiO_3}$-doped $\mathrm{(Bi_{0.5}Na_{0.5})TiO_3}$ piezoelectric ceramics, Journal of Alloys and Compounds 490 (2010) 690–694.

[11] D.L. West, D.A. Payne, Reactive-templated grain growth of Bi-1/2(Na,K)(1/2)TiO3: effects of formulation on texture development, Journal of the American Ceramic Society 86 (2003) 769–774.

[12] J. Richard, G. Pettry, S. Said, P. Marchet, J.P. Mercurio, Sodium-bismuth titanate based lead-free ferroelectric materials, Journal of the European Ceramic Society 24 (2004) 1165–1169.

[13] Q. Xu, S.T. Chen, W. Chen, S.J. Wu, J. Zhou, H.J. Sun, Y.M. Li, Synthesis and piezoelectric and ferroelectric properties of (Na0.5 Bi0.5)(1 x)BaxTiO3 ceramics, Materials Chemistry and Physics 90 (2005) 111–115.

[14] Y. Hiruma, Y. Watanabe, H. Nagata, T. Takenaka., Phase transition temperatures of divalent and trivalent ions substituted $\mathrm{(Bi_{1/2}Na_{1/2})TiO_3}$ Ceramics, Key Engineering Materials 350 (2007) 93.

[15] Y.F. Liu, Y.N. Lu, S.H. Dai, Hydrothermal synthesis of monosized $\mathrm{Bi_{0.5}Na_{0.5}TiO_3}$ spherical particles under low alkaline solution concentration, Journal of Alloys and Compounds 484 (2009) 801–805.

[16] V. Dorcet, G. Trolliard, P. Boullay, Reinvestigation of phase transitions in Na(0.5)Bi(0.5)TiO(3) by TEM. Part I: First order rhombohedral to orthorhombic phase transition, Chemistry of Materials 20 (2008) 5061.

[17] L.A. Schmitt, J. Kling, M. Hinterstein, M. Hoelzel, Wook Jo H.-J. Kleebe, H. Fuess, Structural investigations on lead-free Bi1/2Na1/2TiO3-based piezoceramics, Journal of Materials Science 46 (2011) 4368–4376.

[18] M. Chen, Q. Xu, B.H. Kim, B.K. Ahn, J.H. Ko, W.J. Kang, O.J. Nam, Structure and electrical properties of (Na0.5Bi0.5)1-xBax-TiO3 piezoelectric ceramics, Journal of the European Ceramic Society 28 (2008) 843–849.

[19] M. Barmatz, L.R. Testardi, F.J. di Salvo, Elasticity measurements in layered dichalcogenides TaSe2 and NbSe2, Physical Review B 12 (1975) 4367–4376.